Available online at www.sciencedirect.com
ScienceDirect
International Journal of Heat and Fluid Flow 28 (2007) 768–776
International Journal of HEAT AND FLUID FLOW
www.elsevier.com/locate/ijhff

Melt motion during liquid-encapsulated Czochralski crystal growth in steady and rotating magnetic fields

Mei Yang [a], Nancy Ma [a,*], David F. Bliss [b], George G. Bryant [b]

[a] Department of Mechanical and Aerospace Engineering, North Carolina State University, 2601 Stinson Drive, Campus Box 7910, Raleigh NC 27695, USA
[b] US Air Force Research Laboratory, Sensors Directorate, AFRL/SNHC, 80 Scott Road, Hanscom AFB, MA 01731, USA

Received 19 July 2006; received in revised form 22 August 2006; accepted 25 August 2006
Available online 12 October 2006

Abstract

During the liquid-encapsulated Czochralski (LEC) process, a single compound semiconductor crystal such as gallium-antimonide is grown by the solidification of an initially molten semiconductor (melt) contained in a crucible. The motion of the electrically-conducting molten semiconductor can be controlled with externally-applied magnetic fields. A steady magnetic field provides an electromagnetic stabilization of the melt motion during the LEC process. With a steady axial magnetic field alone, the melt motion produces a radially-inward flow below the crystal–melt interface. Recently, an extremely promising flow phenomenon has been revealed in which a rotating magnetic field induces a radially-inward flow below the crystal–melt interface that may significantly improve the compositional homogeneity in the crystal. This paper presents a model for the melt motion during the LEC process with steady and rotating magnetic fields.

Keywords: Semiconductor crystal growth; Numerical modelling; Magnetic fields; Electromagnetic stirring; Liquid encapsulated Czochralski method; Single crystal growth

1. Introduction

Bulk gallium-antimonide (GaSb) semiconductor crystals with high optical transmission are extremely important for space-based imaging applications. Bulk gallium-antimonide crystals can be grown from the melt by the liquid-encapsulated Czochralski (LEC) process. A major objective during the growth of a semiconductor crystal is to minimize the segregation in the crystal. Since molten semiconductors are excellent electrical conductors, externally-applied magnetic fields can be used to control the melt motion in order to control the dopant distribution in the crystal, which depends on the convective and diffusive transport of the dopant in the melt. Convective transport in the melt may lead to (i) small-scale spatial oscillations of the crystal's dopant composition, which are called striations or microsegregation, and/or (ii) large-scale variations of the crystal's dopant composition, which are called radial and axial macrosegregation.

During the bulk growth of semiconductor crystals without a steady magnetic field, the buoyant convection in the melt is often periodic, or even turbulent in very large systems. Unsteady melt motions lead to fluctuations in the heat transfer across the growth interface from the melt to the crystal. Since the local rate of crystallization depends on the balance between the local heat fluxes in the melt and crystal, fluctuations in the heat flux from the melt create fluctuations in the local growth rate. In extreme circumstances, periods of growth alternate with periods of remelting. Fluctuations in the local growth rate cause two major problems. First, these fluctuations are a major cause of dislocations in the crystal (Kuroda et al., 1984). Another major cause of dislocations is the thermal stresses in the

* Corresponding author. Tel.: +1 919 5155231; fax: +1 919 5157968.
E-mail address: nancy_ma@ncsu.edu (N. Ma).

0142-727X/$ - see front matter © 2006 Elsevier Inc. All rights reserved.
doi:10.1016/j.ijheatfluidflow.2006.08.001

crystal. Second, the fluctuations in the local growth rate create striations in the crystal. Most dopants are either rejected into the melt during solidification or preferentially absorbed into the crystal, i.e. $k_s < 1$ or $k_s > 1$, respectively, where the segregation coefficient k_s is the ratio of the local dopant concentration in the crystal to that in the melt at any point along the crystal–melt interface. If $k_s < 1$, the rejected dopant accumulates in a species-diffusion boundary layer in the melt adjacent to the interface. The dopant distribution in this layer involves a balance between the rejection rate and the rate of diffusion through the melt. During a fluctuation in the local growth rate, an increase in growth rate causes the local concentration to rise because dopant cannot diffuse away fast enough, so that a region with a high dopant concentration solidifies. When the growth rate decreases for the second half of the fluctuation, dopant has ample time to diffuse away, so the concentration that solidifies is low. Fluctuations in the melt velocity also convect dopant in and out of the species-diffusion boundary layer or radially within this layer, leading to more severe striations.

A steady magnetic field produced by a solenoid placed around the crystal-growth furnace can be used to stabilize the melt in order to eliminate all periodicity in the melt motion and to eliminate striations produced by unsteady melt motions (Walker et al., 2002). Without a steady magnetic field, transitions from steady, axisymmetric melt motions to the periodic or even turbulent non-axisymmetric melt motions which produce striations depend upon the ratio of the driving buoyancy force to viscous dissipation, as reflected by the Rayleigh or Grashof number. With a steady moderate magnetic field, both viscous and Joulean dissipations oppose the driving buoyancy force and stabilize the flow through electromagnetic (EM) damping. Bliss et al. (1991, 1993) were the first to produce 8-cm diameter twin-free indium-phosphide crystals by using magnetic stabilization. Li et al. (2006) provided numerical predictions of thermal stress in the crystal during the LEC process and found that the crystal's thermal stress increases as the magnetic field strength increases.

Unfortunately, crystal growth in a steady magnetic field alone produces crystals with relatively severe dopant segregation because there is a radially-inward flow just below the crystal–melt interface (Morton et al., 2002; Morton et al., 2003; Yang et al., 2005). Morton et al. (2002) indicated that the radial and axial segregation decreases as the magnetic field strength decreases. This occurs because the magnitude of the radially-inward flow below the crystal–melt interface increases as the magnetic field strength decreases. A means to tailor the melt motion in order to increase the radially-inward flow below the crystal–melt interface may achieve both radial and axial uniformity in the crystal. Recent experiments have shown that certain periodic, transverse magnetic fields, called rotating magnetic fields (RMFs), produce better crystals with less segregation (Salk et al., 1994; Fiederle et al., 1996). An RMF is a transverse magnetic field with a fixed spatial pattern which rotates at an angular velocity around the vertical centerline of the crucible. An RMF is produced by connecting a number of inductors at equally-spaced azimuthal positions to the successive phases of a multiphase AC power source. Since a steady magnetic field is needed in order to stabilize the melt motion, an RMF would be superimposed on the steady magnetic field. To date, there has been one study which investigated combining an RMF and a uniform, axial, steady magnetic field by presenting a numerical solution for a liquid-metal flow in a fixed cylinder (Mossner and Gerbeth, 1999). Witkowski et al. (1999) and Walker et al. (2004) modelled the flow of electrically-conducting fluids in a vertical cylinder. Walker (1999) reviewed the use of steady magnetic fields during crystal growth while Dold and Benz (1999) reviewed the use of rotating magnetic fields during crystal growth. In the present paper, we treat the buoyant convection and crystal-growth flow during the LEC process in the presence of both steady and rotating magnetic fields.

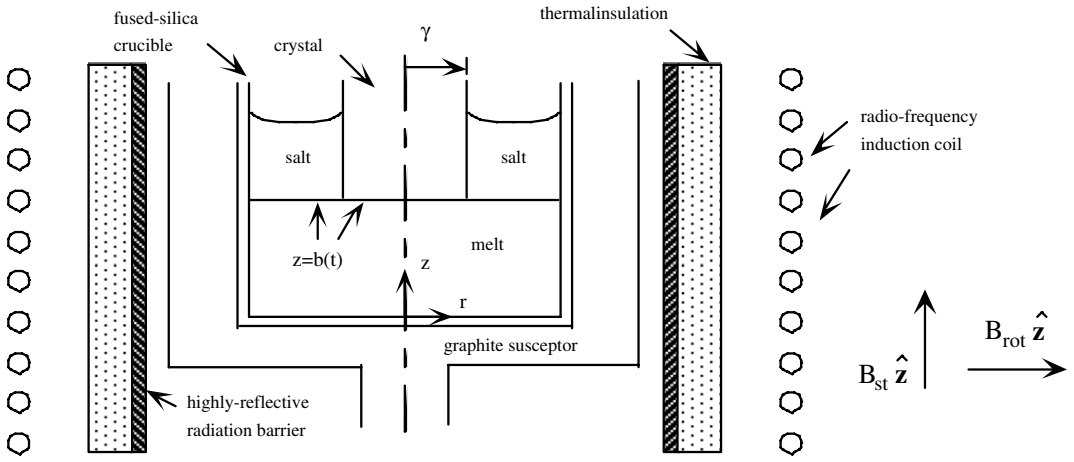

Fig. 1. Liquid-encapsulated Czochralski crystal growth with a uniform steady axial magnetic field $B_{st}\hat{\mathbf{z}}$ with a rotating transverse magnetic field $B_{rot}\hat{\mathbf{x}}$ and with coordinates normalized by the crucible's inner radius.

2. Temperature

This paper treats the unsteady, axisymmetric transport of a gallium-antimonide melt during the liquid-encapsulated Czochralski process with an externally-applied, steady, uniform, axial magnetic field $B_{st}\hat{\mathbf{z}}$ and with an externally-applied, rotating, transverse magnetic field $B_{rot}\hat{\mathbf{x}}$, as shown in Fig. 1. Here, B_{st} and B_{rot} are the flux densities of the steady and rotating magnetic fields, respectively, and $\hat{\mathbf{r}}$, $\hat{\boldsymbol{\theta}}$ and $\hat{\mathbf{z}}$ are the unit vectors for the cylindrical coordinate system while $\hat{\mathbf{x}}$, $\hat{\mathbf{y}}$ and $\hat{\mathbf{z}}$ are the unit vectors for the Cartesian coordinate system. The coordinates and lengths are normalized by the crucible's inner radius R, so that γ is the dimensionless crystal radius, and $b(t)$ is the dimensionless depth of the melt. This study uses the bulk approximation which assumes that the crystal–melt and encapsulant–melt interfaces lie in the same horizontal plane at $z = b(t) = b_0 - \alpha\gamma^2 t$, where t is time normalized with R/U_b. Here, b_0 is the initial dimensionless melt depth and the dimensionless crystal-growth velocity $\alpha = U_g/U_b$ is the sum of the velocity at which the crystal is moved upward and the velocity at which the crystal–melt interface moves downward. Here, U_b is the characteristic velocity of the melt while U_g is the crystal-growth velocity.

Before solidification begins, gallium and antimony are heated in the crucible and the elements fuse to form the compound GaSb. A layer of salt, which is composed of a mixture of 50% sodium-chloride (NaCl) and 50% potassium chloride (KCl), encapsulates the melt. A single crystal seed is lowered through the liquid salt mixture which initiates solidification. Once the crystal has grown to the desired diameter, the crystal is pulled vertically upward at a rate which maintains this diameter. The melt is housed by a fused-silica crucible which is structurally supported by a graphite susceptor as shown in Fig. 1.

The melt velocity is normalized by the characteristic velocity for magnetically damped buoyant convection (Hjellming and Walker, 1987)

$$U_b = \frac{\rho g \beta (\Delta T)_c}{\sigma B_{st}^2}, \tag{1}$$

where $g = 9.81\ \mathrm{m/s^2}$ and $(\Delta T)_c$ is the characteristic temperature difference in the melt. Here, ρ, σ and β are the melt's density at the solidification temperature T_s, the melt's electrical conductivity and the melt's thermal volumetric expansion coefficient, respectively. The crystal–melt interface moves at a constant dimensionless velocity α, and the dimensionless time to grow the entire crystal is $b_0/\alpha\gamma^2$ if the entire melt is solidified.

The temperature is governed by

$$Pe_t\left[\frac{\partial T}{\partial t} + (\mathbf{v}\cdot\nabla)T\right] = \nabla^2 T, \tag{2}$$

where $\mathbf{v}(r,\zeta,t) = v_r\hat{\mathbf{r}} + v_\theta\hat{\boldsymbol{\theta}} + v_z\hat{\mathbf{z}}$ is the dimensionless velocity of the melt normalized by U_b, and T is the deviation of the dimensional temperature from the solidification temperature T_s normalized by $(\Delta T)_c$. In Eq. (2), the characteristic ratio of the convective to conductive heat transfer is the thermal Péclet number, $Pe_t = \rho c_p U_b R/k$, where c_p is the melt's specific heat and k is the melt's thermal conductivity. The thermal Péclet number decreases as B_{st}^{-2}, so that the ratio of the convective heat transfer to conductive heat transfer decreases as the magnetic field strength increases. Ma and Walker (2001) found that the error due to neglect of convective heat transfer is less than 4% when $Pe_t < 15.0$ for which $B_{st} > 0.20\ \mathrm{T}$ for the present process. Since, $U_g < U_b$, the latent heat released by the cooling melt is negligible compared to the conductive heat transfer (Ma and Walker, 1997). Therefore, only the conductive terms are included in the present study.

We use the boundary conditions

$$\frac{\partial T}{\partial \zeta} = -q_b(r,t) \quad \text{at } \zeta = -1, \tag{3a}$$

$$\frac{\partial T}{\partial r} = 1 \quad \text{at } r = 1, \tag{3b}$$

$$T = 0 \quad \text{at } \zeta = +1 \quad \text{for } 0 \leqslant r \leqslant \gamma, \tag{3c}$$

$$\frac{2}{b(t)}\frac{\partial T}{\partial \zeta} = -\kappa_0 \quad \text{at } \zeta = +1 \quad \text{for } \gamma \leqslant r \leqslant 1, \tag{3d}$$

where $q_b(r,t)$ is the dimensionless heat flux into the melt along the bottom crucible wall, and κ_0 is the dimensionless heat flux lost due to conduction and radiation through the semitransparent boron oxide. $q_b(r,t)$ and κ_0 are normalized with $(\Delta T)_c k/R$. Here, $\zeta = -1 + 2z/b(t)$ is a rescaled axial coordinate so that $-1 \leqslant \zeta \leqslant +1$ for all time. An estimate of the thermal losses through the semi-transparent encapsulant (Dupret et al., 1990) give $\kappa_0 = 1.2$.

In the present study, we treat the thermal problem with uniform side heating and with parabolically-varying bottom heating which varies over time so that $0 \leqslant T(r,\zeta,t) \leqslant 1$ for all stages of growth. For LEC growth, the bottom heat-

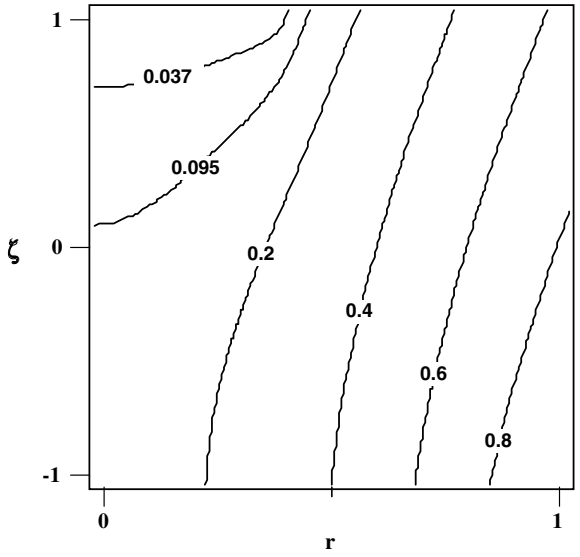

Fig. 2. Temperature in the melt when 50% of the crystal has grown for $\gamma = 0.4$ and $b = 0.3174$.

ing is estimated by a quadratic form given by (Morton et al., 2002)

$$q_b(r,t) = h[b(t)]r^2, \tag{4}$$

where $h[b(t)] = 0.890b + 0.369b^2 - 5.984b^3 + 7.334b^4 - 3.273b^5$.

We use a Chebyshev spectral collocation method to solve for the temperature governed by Eqs. (2) and (3) with Gauss–Lobatto collocation points in r and ζ. A regularization method is implemented to avoid Gibbs phenomena associated with the discontinuous boundary condition at $r = \gamma$ and $\zeta = +1$. Typical isotherms are presented in Fig. 2 for $\gamma = 0.4$ and $b = 0.3174$, which correspond to 50% of growth.

3. Melt motion

We apply a rotating magnetic field (RMF) with a frequency $f = 60$ Hz and with one pair of magnet poles for which $m = 1$. This spatially-uniform, transverse, rotating magnetic field produces an essentially constant magnetic-field pattern which rotates in the azimuthal direction around the vertical centerline of the melt with an angular velocity ω/m, where ω is the circular frequency of the electric power source. An RMF actually produces a periodic, non-axisymmetric body force in addition to the steady, axisymmetric, azimuthal body force but the frequency of the non-axisymmetric body force is $2mf$, and the inertia of the melt precludes any response such a high-frequency oscillatory body force (Witkowski et al., 1999).

The EM body force per unit volume $\mathbf{S}^*$ created by the externally-applied steady and rotating magnetic fields is

$$\mathbf{S}^* = (\mathbf{j}^*_{st} \times B_{st}\hat{\mathbf{z}}) + (\mathbf{j}^*_{rot} \times B_{rot}\hat{\mathbf{x}}) + (\mathbf{j}^*_{st} \times B_{rot}\hat{\mathbf{x}}) + (\mathbf{j}^*_{rot} \times B_{st}\hat{\mathbf{z}}), \tag{5}$$

where $\mathbf{j}^*_{st}$ is the electric current density induced by the static magnetic field and $\mathbf{j}^*_{rot}$ is the electric current density induced by the rotating magnetic field. In Eq. (5), the last two terms, i.e., the electromagnetic body forces created by $\mathbf{j}^*_{st}$ and the rotating magnetic field and by $\mathbf{j}^*_{rot}$ and the static magnetic field, are negligible compared with the first two terms (Mossner and Gerbeth, 1999). In present study, we neglect these two terms. An externally-applied RMF is given by

$$B_{rot}\hat{\mathbf{x}} = B_\omega[\cos(\theta - \omega t)\hat{\mathbf{r}} - \sin(\theta - \omega t)\hat{\boldsymbol{\theta}}], \tag{6}$$

where B_ω is the amplitude of the strength of the rotating magnetic field and t is time normalized by R/U_b.

The electric current in the melt produces an induced magnetic field which is superimposed upon the externally-applied magnetic fields. The characteristic ratio of the induced to steady magnetic field strength is the magnetic Reynolds number, $R_m = \mu_p \sigma U_b R$, where μ_p is the magnetic permeability of the melt. The characteristic ratio of the induced magnetic field to the rotating magnetic field is the shielding parameter, $R_\omega = \mu_p \sigma \omega R^2$. For all crystal-growth processes from the melt, both $R_m \ll 1$ and $R_\omega \ll 1$, so that the additional magnetic fields produced by the electric currents in the melt are negligible. These effects may be important during liquid phase diffusion growth (Yildez et al., 2006).

With the Boussinesq approximation, the equations governing the three-dimensional axisymmetric melt motion are

$$\frac{1}{N}\left[\frac{\partial \mathbf{v}}{\partial t} + (\mathbf{v}\cdot\nabla)\mathbf{v}\right] = -\nabla p + T\hat{\mathbf{z}} + \mathbf{S}_{st} + \frac{T_m \mathrm{Pr}}{Ra}\mathbf{S}_{rot} + \frac{1}{\mathrm{Ha}^2}\nabla^2\mathbf{v}, \tag{7a}$$

$$\nabla\cdot\mathbf{v} = 0, \tag{7b}$$

where p is the deviation of the dimensional pressure from the hydrostatic pressure normalized by $\sigma B_{st}^2 U_b R$, and T is given by a solution to Eqs. (2) and (3). In Eq. (7a), the characteristic ratio of the EM body force induced by the steady field to the inertial force is the interaction parameter, $N = \sigma B_{st} R/\rho U_c$, while the square root of the characteristic ratio of the EM body force induced by the steady field to the viscous force is the Hartmann number, $Ha = B_{st}R(\sigma/\mu)^{1/2}$. The characteristic ratio of the EM body force induced by the RMF to the EM body force induced by the steady field is $T_m Pr/Ra$, where the magnetic Taylor number is $T_m = \rho\sigma\omega B_\omega^2 R^4/\mu^2$, the Prandtl number is $Pr = \mu c_p/k$, and the Rayleigh number is $Ra = g\rho^2 c_p \beta(\Delta T)R^3/\mu k$. The EM body forces per unit volume due to the steady field and due to the rotating field normalized by $\sigma U_b B_{st}^2$ are $\mathbf{S}_{st}$ and $\mathbf{S}_{rot}$, respectively. For electrically-insulating boundaries, these forces are given by

$$\mathbf{S}_{st} = -v_r\hat{\mathbf{r}} - v_\theta\hat{\boldsymbol{\theta}}, \tag{8a}$$

$$\mathbf{S}_{rot} = \left[\frac{r}{2} - \sum_{n=1}^{\infty}\frac{J_1(\lambda_n r)\cosh\left(\frac{b}{2}\lambda_n\zeta\right)}{(\lambda_n^2 - 1)J_1(\lambda_n)\cosh\left(\frac{b}{2}\lambda_n\right)}\right]\hat{\boldsymbol{\theta}}, \tag{8b}$$

where J_k is the Bessel function of the first kind and kth order, and λ_n are the roots of $\lambda_n J_0(\lambda_n) - J_1(\lambda_n) = 0$. Eq. (8b) was originally derived by Witkowski et al. (1999). In

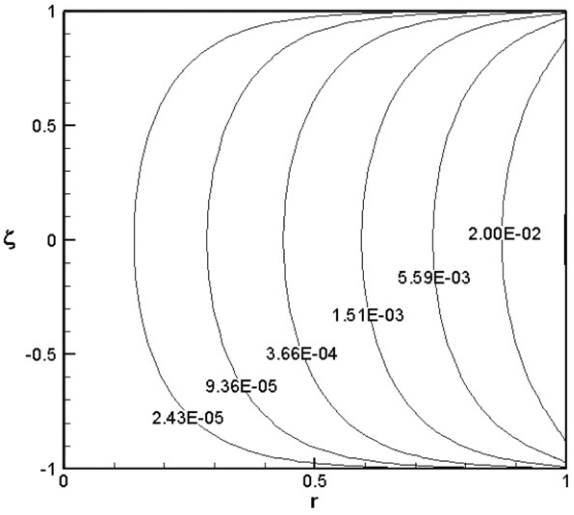

Fig. 3. Magnitude of the azimuthal EM body force per unit volume due to the RMF in the melt $\mathbf{S}_{rot}(r,\zeta)$ when 50% of the crystal has grown for $b = 0.3174$.

Fig. 3, we present contours of the magnitude of the azimuthal EM body force due to the RMF given by Eq. (8b) when 50% of the crystal has grown for $b = 0.3174$. The maximum value occurs at $r = 1$ and $\zeta = 0$, and decreases as r decreases and as $|\zeta|$ increases. In Fig. 3, the maximum value is 0.061932.

We introduce a Stokes streamfunction for the radial and axial velocities in the meridional circulations

$$v_r = \frac{2}{b}\frac{1}{r}\frac{\partial\psi}{\partial\zeta}, \quad v_z = -\frac{1}{r}\frac{\partial\psi}{\partial r}, \tag{9a, 9b}$$

which identically satisfies conservation of mass (7b) for our axisymmetric melt motion. The boundary conditions along the crystal–melt and encapsulant–melt interfaces are

$$\psi = -\frac{1}{2}\alpha(1-\gamma^2)r^2 \quad \text{at } \zeta = +1 \quad \text{for } 0 \leqslant r \leqslant \gamma, \tag{10a}$$

$$\psi = -\frac{1}{2}\alpha\gamma^2(1-\gamma^2)r^2 \quad \text{at } \zeta = +1 \quad \text{for } \gamma \leqslant r \leqslant 1. \tag{10b}$$

During crystal growth, experiments indicate that the liquid salt mixture has an unstable or even turbulent flow. We believe that this occurs because the encapsulant has a very small viscosity compared with that of the melt and because the thermocapillary convection driven by the surface tension's temperature along the interface is negligible compared to the other melt motions for growth in a steady magnetic field (Yang and Ma, 2005a,b; Farrell and Ma, 2002). Therefore, we treat the encapsulant–melt interface as a free surface.

In the melt, there are three mechanisms that drive flow, which are (a) the EM stirring induced by the RMF, (b) the buoyant convection, and (c) the melt-depletion or crystal-growth flow. (a) The azimuthal EM body force due to the RMF induces an azimuthal melt motion. The axial variation of the centrifugal force due to the azimuthal velocity induces a secondary flow in the meridional plane with radial and axial velocity components, v_r and v_z, respectively, which we refer to as the meridional melt motion. The EM stirring alone would be symmetric about the mid-height at $\zeta = 0$, and would induce a clockwise circulation for $\zeta < 0$ and a counterclockwise circulation for $\zeta > 0$. The clockwise circulation would provide a radially-inward flow below the encapsulant–melt and crystal–melt interfaces. (b) Since the melt is heated along its side and bottom, the buoyant convection alone would have a single counterclockwise circulation with radially-inward flow below the interfaces. (c) In a reference frame moving with the crucible, the fluid along the encapsulant–melt interface moves downward at a rate $-\mathrm{d}b/\mathrm{d}t$ while the fluid along the crystal–melt interface moves vertically upward at the pull velocity (Morton et al., 2001), driving a melt motion which is referred to as the melt-depletion flow. This terminology arises because the crystal–melt interface acts as a porous boundary condition. This flow alone would be radially-inward everywhere with axially-downward flow below the encapsulant–melt interface and axially-upward flow below the crystal–melt interface. Each of these three flows produces a radially-inward flow below the crystal–melt interface.

The steady magnetic field provides an EM damping of the radial and azimuthal velocities, as reflected by Eq. (8a). When the electrically-conducting melt flows radially or azimuthally across the steady vertical magnetic field, it generates an induced electric field which drives an azimuthal electric current or a radial electric current, respectively. The azimuthal and radial electric currents flow across the steady magnetic field lines, creating an EM body force which opposes the radial and azimuthal velocities. There is no EM body force opposing flow along steady magnetic field lines.

Therefore, in the present study, we investigate a combination of steady and rotating magnetic fields for which the flow is three dimensional, axisymmetric and stable. Kakimoto (2002) investigate instability of the non-axisymmetric three-dimensional flow during the Czochralski growth of silicon crystals with an RMF and without a steady magnetic field.

We use a Chebyshev spectral collocation method with Gauss–Lobatto collocation points to solve Eqs. (7a) and (7b) with Eqs. (10a) and (10b) along $\zeta = +1$, and the no-slip and no-penetration conditions along the crucible's walls. For the time derivative in Eq. (7a), we use a second-order implicit time integration scheme from $t = 0$ to a t which is slightly less than $b_0/\alpha\gamma^2$. A regularization method is implemented to avoid Gibbs phenomena associated with the discontinuous boundary condition at $r = \gamma$ and $\zeta = +1$. The initial condition at $t = 0$ is given by a solution to Eqs. (7a) and (7b) without the time derivative in Eq. (7a), which is solved using a Newton–Raphson iterative procedure.

4. Results

We present results for several combinations of steady and rotating magnetic fields. For a typical process, $R = 4.7$ cm, $(\Delta T)_c = 20$ K and $U_g = 5.55556 \times 10^{-6}$ m/s. For gallium antimonide, $Pr = 0.0443087$ and $Ra = 5.88992 \times 10^5$. The thermophysical properties for gallium antimonide and the system parameters are summarized in Tables 1 and 2, respectively. Under these conditions, $U_b = 1.13301 \times 10^{-4} B_{st}^{-2}$, $\alpha = 0.0490336 B_{st}^2$, $N = 68793.4 B_{st}^4$, $Ha = 977.894 B_{st}$, and $T_m = 2.07882 \times 10^{12} B_\omega^2$ with B_{st} and B_ω in Tesla. The characteristic ratio of the

Table 1
Thermophysical properties of molten gallium antimonide (GaSb)

Property	Value	Units
Density	6030	kg/m^3
Dynamic viscosity	0.00231	Pa s
Thermal conductivity	17.1	W/m K
Specific heat	328	J/kg K
Thermal volumetric expansion coefficient	0.0000958	K^{-1}
Electrical conductivity	1×10^6	S/m

Table 2
System parameters for liquid-encapsulated Czochralski crystal growth

Parameter	Value	Units
Inner crucible radius, R	4.7	cm
Crystal radius, γR	1.88	cm
Growth rate, U_g	5.556×10^{-6}	m/s
Initial melt depth, $b_o R$	2.98	cm
Characteristic temperature difference, $(\Delta T)_c$	20	K
Frequency of the RMF, f	60	Hz

EM body force induced by the RMF to the EM body force induced by the steady field is $T_m Pr/Ra = 1.56385\times10^5 B_\omega^2$. The characteristic velocities and dimensionless parameters as a function of B_{st} and B_ω are presented in Table 3.

We begin by discussing the effects of an applied RMF. An RMF induces an azimuthal body force which drives a primary flow in the azimuthal direction around the centerline of the melt with an azimuthal velocity v_θ. This azimuthal EM body force $\mathbf{S}_{rot}$ in shown in Fig. 3 for a melt depth $b = 0.3174$ when 50% of the crystal has grown, for example. The actual EM body force due to the RMF is given by the product of $\mathbf{S}_{rot}$ and $T_m Pr/Ra$. The axial variation of the centrifugal force due to the azimuthal velocity induces a secondary flow in the meridional plane with radial and axial velocity components, v_r and v_z, respectively, which we refer to as the meridional melt motion. In the absence of any other flows such as the buoyant convection and the melt-depletion flows, the meridional melt motion due to the EM stirring would be symmetric about the mid-height at $\zeta = 0$, would have a counterclockwise circulation for $\zeta > 0$ with radially-inward flow below the crystal–melt and encapsulant–melt interfaces, and would have a clockwise circulation for $\zeta < 0$ with radially-inward flow adjacent to the bottom of the crucible.

We investigate the effects of increasing B_ω with $B_{st} = 0.5$ T. For $B_{st} = 0.5$ T, the characteristic velocity is $U_b = 0.0004532$ m/s and the dimensionless parameters are $N = 4{,}299.6$, $Ha = 488.95$ and $\alpha = 0.012258$. For $B_\omega = 0.01$ T, $T_m = 2.0788\times10^8$ and $T_m Pr/Ra = 15.639$. We present contours of the azimuthal velocity and the streamfunction in the melt for $b = 0.3174$ when 50% of the crystal has grown in Figs. 4 and 5, respectively. In Fig. 4, the maximum value of v_θ is 1.62944 and occurs near $r = 1$ and at $\zeta = 0$. This relatively weak RMF and corresponding azimuthal velocity has a small effect on the meridional melt motion. In Fig. 5, the minimum and maximum values of the streamfunction are -0.000823738 and

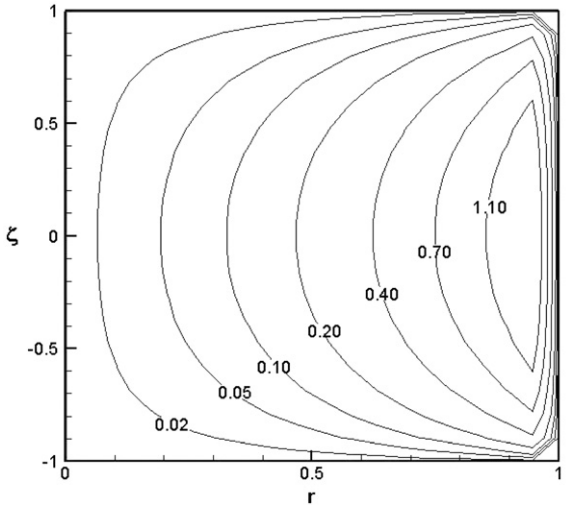

Fig. 4. Azimuthal velocity in the melt $v_\theta(r,\zeta,161.83)$ when 50% of the crystal has grown for $B_{st} = 0.5$ T and $B_\omega = 0.01$ T.

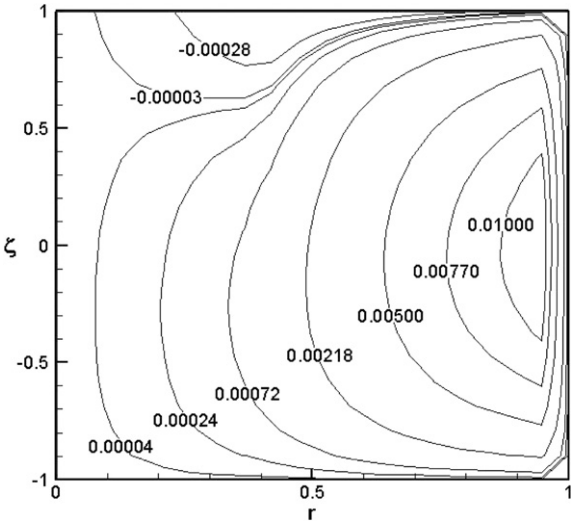

Fig. 5. Streamlines in the melt $\psi(r,\zeta,161.83)$ when 50% of the crystal has grown for $B_{st} = 0.5$ T and $B_\omega = 0.01$ T.

0.0119152, respectively. This maximum value occurs near $r = 1$ and for some value of $\zeta > 0$. This minimum value is due to the melt-depletion flow, as given by Eqs. (10a) or (10b) at $r = \gamma$. Just below the crystal–melt interface at $\zeta = +1$, the flow is dominated by the melt-depletion flow as reflected by the -0.00028 and -0.00003 contours, as shown in Fig. 4. Most of the melt is dominated by a

Table 3
Characteristic velocity and dimensionless parameters for liquid-encapsulated Czochralski crystal growth in steady and rotating magnetic fields

B_{st} (T)	B_ω (T)	U_b (m/s)	α	Ha	T_m	Pr	Ra
0.5	0.01	0.0004532	0.012258	488.95	2.0788×10^8	0.0443087	5.88992×10^5
0.5	0.05	0.0004532	0.012258	488.95	5.1970×10^9	0.0443087	5.88992×10^5
0.5	0.10	0.0004532	0.012258	488.95	2.0788×10^{10}	0.0443087	5.88992×10^5
1.0	0.01	0.0001133	0.049034	977.89	2.0788×10^8	0.0443087	5.88992×10^5
1.0	0.05	0.0001133	0.049034	977.89	5.1970×10^9	0.0443087	5.88992×10^5
1.0	0.10	0.0001133	0.049034	977.89	2.0788×10^{10}	0.0443087	5.88992×10^5

Table 4
Dimensional radial velocity in the melt below the crystal–melt interface $v_r^*(r, \zeta = 0.9999, t = 161.83)$ versus r when 50% of the crystal has grown for $B_{st} = 0.5$ T with $B_\omega = 0.01$ T, 0.05 T and 0.10 T in μm/s

r	$v_r^*(r, 0.9999, 161.83)$ for $B_\omega = 0.01$ T	$v_r^*(r, 0.9999, 161.83)$ for $B_\omega = 0.05$ T	$v_r^*(r, 0.9999, 161.83)$ for $B_\omega = 0.10$ T
0.000000	0.0000	0.0000	0.0000
0.021053	0.8919	0.8430	0.1210
0.042105	−2.9304	−2.9957	−3.9931
0.063158	−2.3063	−2.4214	−4.1477
0.084211	−1.2943	−1.4634	−3.9873
0.105263	−5.0953	−5.2870	−8.1771
0.126316	−4.8198	−5.0663	−8.7730
0.147368	−3.5359	−3.8490	−8.5360
0.168421	−7.1932	−7.5426	−12.8015
0.189474	−7.5684	−7.9836	−14.2337
0.210526	−5.9134	−6.4173	−13.9717
0.231579	−9.1429	−9.7085	−18.2146
0.252632	−10.5931	−11.2439	−21.0380
0.273684	−8.6906	−9.4642	−21.0693
0.294737	−10.8560	−11.7365	−24.9568
0.315789	−13.6363	−14.6352	−29.6633
0.336842	−12.2532	−13.4229	−30.9876
0.357895	−12.4403	−13.7913	−34.0693
0.378947	−15.3272	−16.8618	−39.9292
0.400000	−15.8575	−17.6295	−44.2613

counterclockwise circulation due to buoyant convection. The flow is radially inward below the crystal–melt interface and the dimensional radial velocity at $\zeta = 0.9999$ is presented in Table 4.

For $B_{st} = 0.5$ T, we further increase the flux density of the RMF to $B_\omega = 0.05$ T. For $B_\omega = 0.05$ T, $T_m = 5.1970 \times 10^9$ and $T_m Pr/Ra = 390.96$, so that the relative importance of EM body force due to the RMF to the EM body force due to the steady field increases. For this larger RMF, the contours of the azimuthal velocity are very similar to those shown in Fig. 4, except that the values are larger, with a maximum value equal to 40.7268. This EM stirring has a much stronger effect on the meridional melt motion. We present the meridional streamfunction in Fig. 6, for which the minimum and maximum values are −0.000823738 and 0.0189049, respectively. Since the RMF alone would produce a counterclockwise circulation for $\zeta > 0$, the EM stirring augments the melt-depletion flow and the buoyant convection so that the magnitude of the radially-inward flow below the crystal–melt interface increases, the location of the maximum value of ψ moves vertically upward and the maximum value of ψ increases. The radial velocity just below the crystal–melt interface at $\zeta = 0.9999$ is presented in Table 4 and has increased for this larger value of B_ω. The minimum value of ψ still occurs due to the melt-depletion flow. Since the RMF alone would produce a clockwise circulation for $\zeta < 0$, the EM stirring opposes the buoyant convection for $\zeta < 0$ and becomes strong enough to induce a clockwise circulation near $r = 1$ and $\zeta = -1$, as shown in Fig. 6.

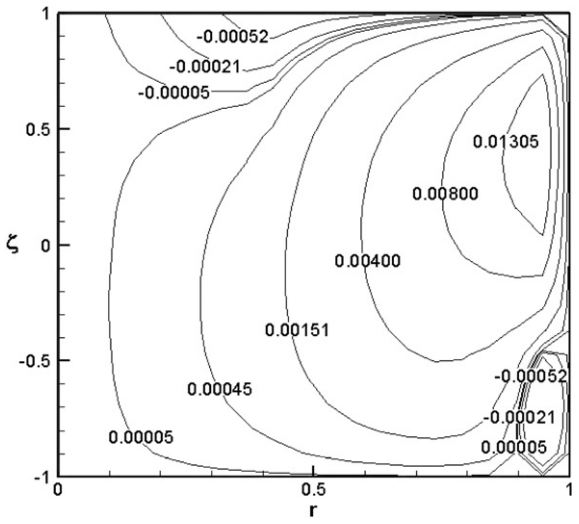

Fig. 6. Streamlines in the melt $\psi(r, \zeta, 161.83)$ when 50% of the crystal has grown for $B_{st} = 0.5$ T and $B_\omega = 0.05$ T.

For $B_{st} = 0.5$ T, we further increase the flux density of the RMF to $B_\omega = 0.10$ T. For $B_\omega = 0.10$ T, $T_m = 2.0788 \times 10^{10}$ and $T_m Pr/Ra = 1563.8$, and relative importance of the EM body force due to the RMF to the EM body force due to the steady field further increases. For this value of B_ω, the maximum value of v_θ increases to 162.376. The EM stirring due to the RMF has a much stronger effect on the meridional melt motion, as shown in Fig. 7. The magnitude of the radially-inward flow below the crystal–melt interface increases significantly as shown in Table 4, and the maximum value of the streamfunction is much larger with $\psi_{max} = 0.165163$. At $r = \gamma$ and $\zeta = +1$, the streamfunction is still equal to −0.000823738 but the minimum value now occurs in the lower clockwise circulation with $\psi_{min} = -0.149373$.

We investigate the effects of increasing B_ω with $B_{st} = 1.0$ T. For $B_{st} = 1.0$ T, the characteristic velocity is $U_b = 0.0001133$ m/s and the dimensionless parameters are

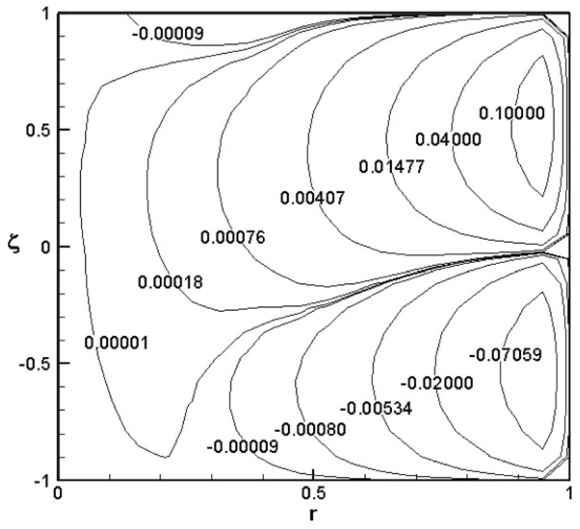

Fig. 7. Streamlines in the melt $\psi(r,\zeta,161.83)$ when 50% of the crystal has grown for $B_{st}=0.5$ T and $B_\omega=0.10$ T.

$N=68{,}793$, $Ha=977.89$ and $\alpha=0.049034$. This steady field provides a much stronger EM damping of the flow so that the RMF has a much weaker effect on the melt motion. For $B_\omega=0.01$ T, the azimuthal velocity is very weak and the meridional melt motion resembles the melt motion with a 1.0 T steady field alone (Morton et al., 2002; Yang, 2006). For $B_\omega=0.01$ T, the meridional melt motion is dominated by the counterclockwise buoyant convection except in an extremely thin region below the crystal–melt interface where the melt motion is dominated by the melt-depletion flow. We present the values for the dimensional radial velocity in the melt just below the crystal–melt interface at $\zeta=0.9999$ in Table 5. When we increase $B_\omega=0.05$ T, the RMF drives a stronger radially inward flow below the crystal–melt interface, as reflected in Table 5. When we increase $B_\omega=0.10$ T, the RMF has a much more pronounced effect with a small clockwise circulation near $r=1$ and $\zeta=-1$. The magnitude of the radial velocity just below the crystal–melt interface is further increased as reflected in Table 5.

Yang (2006) presented the azimuthal velocity and meridional streamfunction corresponding to 5%, 50% and 90% growth for $B_{st}=0.5$ T with $B_\omega=0.01$ T, 0.05 T and 0.10 T and for $B_{st}=1.0$ T with $B_\omega=0.01$ T, 0.05 T and 0.10 T. Yang (2006) found (1) for a given growth rate and RMF, the driving mechanisms for the melt-depletion flow and electromagnetic stirring are constant while the buoyant convection decreases as growth progresses so that the magnitude of the radially-inward flow below the crystal–melt interface decreases as growth progresses, (2) for a given steady magnetic field, increasing the flux density of the RMF increases the magnitude of the radially-inward flow, and (3) for a given RMF, increasing the flux density of the steady magnetic field decreases the magnitude of the radially-inward flow because the steady field provides an electromagnetic damping of the radial component of flow.

5. Conclusions

An externally-applied RMF alone would induce flow in a meridional plane which consists of a counterclockwise circulation in the upper half of the melt below the crystal–melt and encapsulant–melt interfaces and a clockwise circulation in the lower half of the melt. Therefore, the flow induced by the RMF augments the radially-inward flow below the crystal–melt interface due to both the melt-depletion flow and buoyant convection. For a given growth rate

Table 5
Dimensional radial velocity in the melt below the crystal–melt interface $v_r^*(r,\zeta=0.9999,t=40.46)$ versus r when 50% of the crystal has grown for $B_{st}=1.0$ T with $B_\omega=0.01$ T, 0.05 T and 0.10 T in μm/s

r	$v_r^*(r,0.9999,40.46)$ for $B_\omega=0.01$ T	$v_r^*(r,0.9999,40.46)$ for $B_\omega=0.05$ T	$v_r^*(r,0.9999,40.46)$ for $B_\omega=0.10$ T
0.000000	0.0000	0.0000	0.0000
0.021053	1.3232	1.3226	1.3124
0.042105	−2.1272	−2.1283	−2.1449
0.063158	−1.0272	−1.0290	−1.0561
0.084211	0.4725	0.4700	0.4316
0.105263	−2.9307	−2.9338	−2.9799
0.126316	−2.1715	−2.1754	−2.2336
0.147368	−0.3765	−0.3813	−0.4534
0.168421	−3.6165	−3.6221	−3.7050
0.189474	−3.4973	−3.5039	−3.6020
0.210526	−1.2895	−1.2973	−1.4141
0.231579	−4.0646	−4.0735	−4.2069
0.252632	−5.0110	−5.0212	−5.1752
0.273684	−2.4988	−2.5108	−2.6911
0.294737	−4.1467	−4.1604	−4.3669
0.315789	−6.4363	−6.4521	−6.6882
0.336842	−4.4226	−4.4408	−4.7149
0.357895	−4.0616	−4.0825	−4.3986
0.378947	−6.7690	−6.7930	−7.1546
0.400000	−6.9872	−7.0150	−7.4320

and RMF, the driving mechanisms for the melt-depletion flow and electromagnetic stirring are constant while the buoyant convection decreases as growth progresses so that the magnitude of the radially-inward flow below the crystal–melt interface decreases as growth progresses. For a given steady magnetic field, increasing the flux density of the RMF increases the magnitude of the radially-inward flow. For a given RMF, increasing the flux density of the steady magnetic field decreases the magnitude of the radially-inward flow because the steady field provides an electromagnetic damping of the radial component of flow. The addition of the RMF may be beneficial for reducing segregation in the crystal because it may help convect the dopant away from the crystal–melt interface.

Acknowledgements

This research was supported by the US Air Force Office of Scientific Research under grant FA9550-04-1-0249. The calculations were performed on the Cray X1 provided by the DoD High Performance Computing Modernization Program under grant AFSNH2487 and on the IBM pSeries 690 provided by the National Computational Science Alliance.

References

Bliss, D.F., Hilton, R.M., Bachowski, S., Adamski, J.A., 1991. MLEK crystal growth of (100) indium phosphide. Journal of Electronic Materials 20, 967–971.

Bliss, D.F., Hilton, R.M., Adamski, J.A., 1993. MLEK crystal growth of large diameter (100) indium phosphide. Journal of Crystal Growth 128, 451–456.

Dold, P., Benz, K.W., 1999. Rotating magnetic fields: fluid flow and crystal growth applications. Progress in Crystal Growth and Characterization of Materials 38, 7–38.

Dupret, F., Nicodème, P., Ryckmans, Y., Crochet, M.J., 1990. Global modelling of heat transfer in crystal growth furnaces. International Journal of Heat and Mass Transfer 3, 1849–1870.

Farrell, M.V., Ma, N., 2002. Coupling of buoyant convections in boron oxide and a molten semiconductor in a vertical magnetic field. Journal of Heat Transfer 124, 643–649.

Fiederle, M., Eiche, C., Joergerm, W., Salk, M., Senchenkov, A.S., Egorov, A.V., Ebling, D.G., Benz, K.W., 1996. Radiation detector properties of $CdTe_{0.9}Se_{0.1}$:Cl crystals grown under microgravity in a rotating magnetic field. Journal of Crystal Growth 166, 256–260.

Hjellming, L.N., Walker, J.S., 1987. Melt motion in the Czochralski crystal puller with an axial magnetic field: motion due to buoyancy and thermocapillarity. Journal of Fluid Mechanics 182, 335–368.

Kakimoto, K., 2002. Effects of rotating magnetic fields on temperature and oxygen distributions in silicon melt. Journal of Crystal Growth 237, 1785–1790.

Kuroda, E., Kozuka, H., Takano, Y., 1984. The effect of temperature oscillations at the growth interface on crystal perfection. Journal of Crystal Growth 68, 613–623.

Li, M., Liu, C., Wang, P., 2006. Numerical simulation of LEC growth of InP crystal with an axial magnetic field. International Journal of Heat and Mass Transfer 49, 1738–1746.

Ma, N., Walker, J.S., 1997. Dopant transport during semiconductor crystal growth with magnetically damped buoyant convection. Journal of Crystal Growth 172, 124–135.

Ma, N., Walker, J.S., 2001. Inertia and thermal convection during crystal growth with a steady magnetic field. Journal of Thermophysics and Heat Transfer 15, 50–54.

Morton, J.L., Ma, N., Bliss, D.F., Bryant, G.G., 2001. Diffusion-controlled dopant transport during magnetically-stabilized liquid-encapsulated Czochralski growth of compound semiconductor crystals. Journal of Fluids Engineering 123, 893–898.

Morton, J.L., Ma, N., Bliss, D.F., Bryant, G.G., 2002. Dopant segregation during liquid-encapsulated Czochralski crystal growth in a steady axial magnetic field. Journal of Crystal Growth 242, 471–485.

Morton, J.L., Ma, N., Bliss, D.F., Bryant, G.G., 2003. Magnetic field effects during liquid-encapsulated Czochralski growth of doped photonic semiconductor crystals. Journal of Crystal Growth 250, 174–182.

Mossner, R., Gerbeth, G., 1999. Buoyant melt flows under the influence of steady and rotating magnetic fields. Journal of Crystal Growth 197, 341–354.

Salk, M., Fiederle, M., Benz, K.W., Senchenkov, A.S., Egorov, A.V., Matioukhin, D.G., 1994. CdTe and $CdTe_{0.9}Se_{0.1}$ crystals grown by the traveling heater method using a rotating magnetic-field. Journal of Crystal Growth 138, 161–167.

Walker, J.S., 1999. Models of melt motion, heat transfer and mass transport during crystal growth with strong magnetic fields. Progress in Crystal Growth and Characterization of Materials 38, 195–213.

Walker, J.S., Henry, D., BenHadid, H., 2002. Magnetic stabilization of the buoyant convection in the liquid-encapsulated Czochralski process. Journal of Crystal Growth 243, 108–116.

Walker, J.S., Volz, M.P., Mazuruk, K., 2004. Rayleigh–Bénard instability in a vertical cylinder with a rotating magnetic field. International Journal of Heat and Mass Transfer 47, 1877–1887.

Witkowski, L.M., Walker, J.S., Marty, P., 1999. Nonaxisymmetric flow in a finite-length cylinder with a rotating magnetic field. Physics of Fluids 11, 1821–1826.

Yang, M., 2006. Liquid-encapsulated Czochralski growth of compound semiconductor crystals with steady and rotating magnetic fields. Ph.D. Dissertation, North Carolina State University.

Yang, M., Ma, N., 2005a. Free convection in a liquid-encapsulated molten semiconductor in a vertical magnetic field. International Journal of Heat and Mass Transfer 48, 4010–4018.

Yang, M., Ma, N., 2005b. A computational study of natural convection in a liquid-encapsulated molten semiconductor with a horizontal magnetic field. International Journal of Heat and Fluid Flow 26, 810–816.

Yang, M., Ma, N., Bliss, D.F., Morton, J.L., 2005. Liquid-encapsulated Czochralski growth of doped gallium-antimonide semiconductor crystals using a strong steady magnetic field. Magnetohydrodynamics 41, 73–86.

Yildez, E., Dost, S., Yildez, M., 2006. A numerical simulation study for the effect of magnetic fields in liquid phase diffusion growth of SiGe single crystals. Journal of Crystal Growth 291, 497–511.